INTERNATIONAL JOURNAL FOR NUMERICAL METHODS IN FLUIDS, VOL. 22, 393–409 (1996)

COLLOCATION METHOD FOR CONVECTIVE FLOW INDUCED BY DIRECTIONAL SOLIDIFICATION IN A CYLINDER

C. LE MAREC AND R. GUÉRIN

Laboratoire MATOP, Associé au CNRS, Université d'Aix-Marseille III, Faculté des Sciences de St. Jérôme, Case 151, F-13397 Marseille Cedex 20, France

AND

P. HALDENWANG

Laboratoire de Recherche en Combustion, URA, CNRS 1117, Université de Provence, Faculté des Sciences de St Jérôme, Case 252, F-13397 Marseille Cedex 20, France

SUMMARY

The paper presents a Chebyshev–Fourier collocation method for solving the unsteady 3D Navier–Stokes equations in a cylindrical domain. The numerical scheme uses primitive variables and the incompressibility constraint is satisfied by applying iteratively a correction to the pressure field. The method, due to Cahouët and Chabard (*Int. j. numer. methods fluids*, **8**, 869–895 (1988)) and originally developed in the framework of finite elements, is checked with respect to the present high-order approach. Several tests are carried out in Cartesian geometries, successively 2D and 3D, then a comparison is performed in a cylindrical domain with two different sets of radial collocation nodes: Gauss-Lobatto nodes and Gauss-Radau points. Although quite acceptable results are obtained with the latter chain, a general decrease in efficiency is noticeable in the collocation method. This is interpreted as the consequence of two factors: the collocation formulation is not symmetric and the Fourier analysis, used as heuristic guide by Cahouët and Chabard, loses its efficiency in a non-equidistant grid, especially in a cylindrical geometry.

We present an application to the study of thermosolutal convection induced by unidirectional solidification of a binary alloy. The latter grows from a Pb–30%Tl liquid phase in a cylindrical crucible corresponding to the vertical Bridgman upward configuration. We study the influence of the flow patterns on the crystal composition.

KEY WORDS: generalized Stokes problem; Chebyshev spectral method; thermosolutal convection; directional solidification; vertical Bridgman problem

1. INTRODUCTION

The solidification process is of great interest in material processing. Crystal growth from the molten phase induces concentration and thermal modifications that in turn are responsible for free convective patterns. It is currently accepted that the coupling of the fluid flow with the solidification process is important, because a noticeable influence of the convective patterns on the crystal morphology has been observed.[1–3] Consequently, this coupling has been the subject of several studies, both experimental and theoretical.[4–8]

The present work is concerned with the numerical study of flow patterns in the liquid phase. More precisely, we numerically compute the natural convection accompanying the growth of a binary alloy in a cylindrical crucible. The mathematical model is composed of the Navier–Stokes equations in the

CCC 0271–2091/96/050393–17

Received February 1995
Revised May 1995

Boussinesq approximation, including the conservation laws of heat and solute. This classical set of partial differential equations is completed with boundary conditions specific to directional solidification, namely non-zero velocity of the flow and mixed conditions on the solute concentration at the solid–liquid interface.

The first approaches to this problem involved more classical numerical schemes such as finite differences or finite elements.[9–11] Because natural convection is generated in small length scales (the convective boundary layers), high-accuracy methods have also been chosen. Therefore, in the field of free convection, spectral or pseudospectral methods[12–17] have already been used. The approach currently implemented is the vorticity–streamfunction formulation.[12–17] In order to provide boundary conditions on the vorticity equations, an influence matrix technique is developed.[18,19] Influence matrices are also implemented[20] in the framework of primitive variables to furnish boundary conditions on the pressure field. This technique leads, especially in the 3D case, to matrices of huge size. Its application is limited to problems with rather few degrees of freedom.

To overcome the latter limitation, other authors have proposed[21,22] an iterative solution of the generalized Stokes problem that appears when a semi-implicit treatment is applied to the velocity–pressure formulation. One of these proposals[21] is linked to a Cartesian geometry and cannot be used in our cylindrical approach. Consequently, we have chosen the Cahouët and Chabard[22] algorithm which is of general use. The latter method is concerned with a specific preconditioning of the Uzawa operator that solves the pressure field. Cahouët and Chabard[22] proposed their method in the framework of finite elements, which leads[23] to a symmetrical formulation of the Uzawa operator. Moreover, these authors suggested that their preconditioning should be 'optimal' when an equidistant mesh is used. It is, however, well known that Chebyshev spectral methods suffer from the following two drawbacks: the formulation is not symmetric and the collocation points are not equally spaced. Therefore our purpose is to check the behaviour of the Cahouët and Chabard algorithm when their preconditioning is not supposed to be 'optimum' and the conjugate gradient method cannot be applied. As a result, a loss of efficiency will clearly be observed. Nevertheless, the algorithm remains quite practicable, as shown by the reported illustrations of flow patterns.

Concerning the space discretization with the Chebyshev collocation method, we have chosen Gauss–Lobatto nodes[16] in the axial direction, while equidistant collocation points are selected on the azimuth.[17] For the radial discretization we have compared two sets of collocation points: Gauss–Lobatto nodes (excluding the centre $r = 0$) and Gauss-Radau points. A semi-implicit treatment has been applied for time stepping. It includes the stability preservation technique,[24] the implementation of which is imperative in a cylindrical geometry. This leads to a separate set of elliptic Helmholtz equations and the pressure correction is obtained through a Poisson equation. Therefore we have used the technique[25] of partial diagonalization in each direction in order to solve this sequence of elliptic problems appearing as the implicit parts of the time treatment.

The last part of this paper is concerned with numerical experiments. The selected configuration is the vertical Bridgman problem of directional solidification. We present results relative to three-dimensional flows in a cylinder induced by the growth of a Pb–Tl alloy. Particular attention will be devoted to studying the dependence of the compound flow patterns on the composition of the solid phase.

2. COLLOCATION METHOD IN CYLINDER

2.1. *Mathematical model*

It is a fact that the shape of the solid–liquid interface is a relatively important factor in crystal quality. Nevertheless, we have deliberately chosen to increase the accuracy of the flow computation rather than to consider the feedback of the shape deformation on the flow. As a result, for the time being we have assumed a flat solid–liquid interface. We therefore focus our attention on the convective coupling between the flow and the crystal growth in a non-deformable cylindrical domain, neglecting the coupling between the flow and the eventual deformation of the latter computational domain.

The equations of motion reduced with the length scale D/V_0 and the time scale D/V_0^2 (V_0 is the growth velocity and D is the coefficient of solute diffusion) are

$$\frac{1}{Sc}\frac{\partial \mathbf{V}}{\partial t}+\frac{1}{Sc}(\mathbf{V}\cdot\nabla)\mathbf{V} = -\nabla p + \Delta\mathbf{V} + R_{\mathrm{T}} T\mathbf{e}_z + R_{\mathrm{S}} C\mathbf{e}_z \tag{1}$$

$$\nabla\cdot\mathbf{V} = 0, \tag{2}$$

$$\frac{\partial T}{\partial t} + (\mathbf{V}\cdot\nabla)T = Le\Delta T, \tag{3}$$

$$\frac{\partial C}{\partial t} + (\mathbf{V}\cdot\nabla)C = \Delta C, \tag{4}$$

where R_{T} and R_{S} are the thermal and solutal Rayleigh numbers respectively, Sc is the Schmidt number and Le is the Lewis number. A complete definition of these non-dimensional parameters is furnished in Section 4. In the latter section we additionally discuss the boundary conditions adapted to solidification problems.

2.2. *Time discretization*

The time discretization makes use of the Adams–Bashforth second-order backward Euler scheme[15] described in the following section for the heat equation (3):

$$\left(\frac{\partial T}{\partial t}\right)^{n+1} + [(\mathbf{V}\cdot\nabla)T]^{n+1} = Le(\Delta T)^{n+1}, \tag{5}$$

$$\frac{3}{2\delta t}T^{n+1} - \frac{2}{\delta t}T^{n} + \frac{1}{2\delta t}T^{n-1} - Le\Delta T^{n+1} = -2(\mathbf{V}^{n}\cdot\nabla)T^{n} + (\mathbf{V}^{n-1}\cdot\nabla)T^{n-1} \tag{6}$$

This leads to the Helmholtz elliptic problem

$$\left(\frac{3}{2\delta t} - Le\Delta\right)T^{n+1} = \frac{2T^{n}}{\delta t} - \frac{1}{2\delta t}T^{n-1} - 2(\mathbf{V}^{n}\cdot\nabla)T^{n} + (\mathbf{V}^{n-1}\cdot\nabla)T^{n-1}, \tag{7}$$

which can be written by setting

$$F^{n,n-1} = \frac{1}{Le}\left(\frac{2}{\delta t}T^{n} - \frac{1}{2\delta t}T^{n-1} - 2(\mathbf{V}^{n}\cdot\nabla)T^{n} + (\mathbf{V}^{n-1}\cdot\nabla)T^{n-1}\right) \tag{8}$$

in the compact form

$$\left(\frac{3}{2Le\delta t} - \Delta\right)T^{n+1} = F^{n,n-1}. \tag{9}$$

A similar Helmholtz equation for the concentration can be derived at time $(n+1)\delta t$. For the velocity we obtain the so-called generalised Stokes problem

$$\begin{aligned} \left(\frac{3}{2Sc\delta t} - \Delta\right)\mathbf{V}^{n+1} + \nabla p^{n+1} &= \mathbf{G}^{n,n-1}, \\ \nabla\cdot\mathbf{V}^{n+1} &= 0, \end{aligned} \tag{10}$$

where $\mathbf{G}^{n,n-1}$ is related to the velocity fields at times $n\delta t$ and $(n-1)\delta t$, similar to equation (8). We stress the fact that the global time scheme is of second order.

2.3. *Collocation method*

We have selected a high-precision space discretization method: both axial and radial directions use Chebyshev collocation methods, while Fourier collocation is performed on the azimuth. From equation (9) we have to solve

$$(\sigma I - \Delta)u(r,\theta,z) = f(r,\theta,z), \quad \text{where } (r,\theta,z) \in\,]0,R] \times [0,2\pi[\, \times [0,E_z]. \tag{11}$$

We simply map $]0,R] \times [0,2\pi[\, \times [0,E_z]$ onto $]-1,1] \times [0,2\pi[\, \times [-1,1]$. The boundary conditions we have to face are the most general: Dirichlet, Neumann or mixed types (Robin). The scalar field u is a function of the variables r (radius of cylinder), θ (azimuth) and z (vertical direction). In equation (11) σ is a positive constant. In cylindrical co-ordinates the scalar Laplacian operator reads

$$\Delta u = \left[\frac{1}{r}\frac{\partial}{\partial r}\left(r\frac{\partial}{\partial r}\right) + \frac{1}{r^2}\frac{\partial^2}{\partial\theta^2} + \frac{\partial^2}{\partial z^2}\right]u. \tag{12}$$

Therefore, in contrast with the Cartesian case, equation (11) does not present a separate differential form relative to r and θ. Moreover, to overcome the singularity at $r=0$ (axis of cylinder), we multiply equation (11) by r^2:

$$\left\{\sigma r^2 - \left[r\frac{\partial}{\partial r}\left(r\frac{\partial}{\partial r}\right) + \frac{\partial^2}{\partial\theta^2} + r^2\left(\frac{\partial^2}{\partial z^2}\right)\right]\right\}u = r^2 f. \tag{13}$$

Now the lack of separation is between r and z. We shall explain later the reason for this preference.

In the axial direction z we have considered the Chebyshev–Gauss–Lobatto collocation points defined by

$$\eta_k = \cos\left(\frac{\pi k}{N}\right), \quad 0 \leqslant k \leqslant N.$$

Let us recall that this collocation chain corresponds to the extrema of the Chebyshev polynomial of degree N. In the azimuthal direction we have chosen the set of equidistant collocation points defined by

$$\theta_j = \frac{2\pi j}{M}, \quad 0 \leqslant j \leqslant M-1,$$

$(M-2)/2$ being the number of Fourier modes required for the approximation on the azimuth. In the radial direction two chains of collocation points have been studied. On the one hand the Chebyshev–Gauss–Lobatto points have been considered:

$$\eta_i = \cos\left(\frac{\pi i}{L}\right), \quad 0 \leqslant i \leqslant L-1.$$

On the other hand the Chebyshev–Gauss–Radau points have also been implemented:

$$\eta_i = \cos\left(\frac{2\pi i}{2L-1}\right), \quad 0 \leqslant i \leqslant L-1.$$

The approximation of u is given by

$$u_{LMN}(r, \theta, z) = \sum_{i=0}^{L-1} \sum_{j=0}^{M-1} \sum_{k=0}^{N} u(\eta_i, \theta_j, \eta_k) l_{\eta_i}^{L-1}(r) \phi_{\theta_j}^{M}(\theta) l_{\eta_k}^{N}(z), \tag{14}$$

$$l_{\eta_i}^{P}(x) = \prod_{k=0, k \neq i}^{P} \frac{x - \eta_k}{\eta_i - \eta_k}, \tag{15a}$$

$$\phi_{\theta_j}^{M}(\theta) = \frac{1}{M} \sum_{p=-M/2}^{M/2-1} e^{ip(\theta - \theta_j)}. \tag{15b}$$

$L - 1$, $(M - 2)/2$ and N are the orders of the polynomial (ordinary or trigonometric) approximation by interpolation of u in the directions r, θ and z respectively.

At this point, to solve equation (11), we follow the procedure of complete diagonization of the Helmholtz operator as described in Reference 25. For this purpose we denote

$$\Delta_z = -\frac{\partial^2}{\partial z^2}. \tag{16}$$

Let us mention that this differential operator is equipped with boundary conditions of mixed type. Consequently, it is an invertible discrete operator represented by a matrix of rank $N - 1$ when both unknowns at the extremities of the interval $[-1, 1]$ are preliminary eliminated.[25] Furthermore, the diagonalization of the corresponding matrix, also denoted Δ_z, gives

$$\Delta_z = H_z \Lambda_z H_z^{-1}, \tag{17}$$

where H_z and Λ_z are the matrix formed by the eigenvectors and the diagonal matrix of the eigenvalues of Δ_z respectively. Let us stress that the eigenvalues are real and denoted λ_{zk}, $k = 1, \ldots, N - 1$. Let us now consider the differential part of equation (13) that involves the coupled directions r and z. On the basis of the diagonalization of Δ_z this operator simply reads

$$(\Delta_{rz})_k = (\sigma + \lambda_{zk})r^2 - r\frac{\partial}{\partial r}\left(r\frac{\partial}{\partial r}\right), \quad 1 \leqslant k \leqslant N - 1. \tag{18}$$

The $N - 1$ partial operators $(\Delta_{rz})_k$ require one boundary condition at $r = 1$ to be invertible. Then they can be separately diagonalized in the following form involving matrices of rank $L - 1$ (after elimination of the unknown at $r = 1$):

$$(\Delta_{rz})_k = H_{rk} \Lambda_{rk} H_{rk}^{-1}. \tag{19}$$

Note that the coupling between r and z implies $2(N - 1)$ matrices of rank $L - 1$ for performing the change of basis. Let us emphasize that for both studied collocation chains the eigenvalues are real. If the multiplication by r^2 in equation (13) were omitted, some of these eigenvalues would be complex. The use of real quantities explains our choice in equation (13). The last direction is concerned with the uncoupled variable θ and the partial diagonalization is straightforward, because no boundary conditions are to be treated. Therefore set

$$\Delta_\theta = -\frac{\partial^2}{\partial \theta^2}. \tag{20}$$

The diagonalization gives

$$\Delta_\theta = H_\theta \Lambda_\theta H_\theta^{-1}. \tag{21}$$

Equation 13 then becomes

$$[H_z(R^2)^{-1}H_\theta H_{rk}(\Lambda_{rk}+\Lambda_\theta)H_{rk}^{-1}H_\theta^{-1}H_z^{-1}]\mathbf{U}=\mathbf{S}. \tag{22}$$

R^2 is the diagonal matrix corresponding to the multiplication by r^2. **U** contains the internal unknowns and is a vector of length $(L-1)M(N-1)$. **S** corresponds to a source vector of the same size, composed of the values of the right-hand side of equation (13) expressed at the internal collocation nodes. **S** also includes complementary terms due to the successive eliminations of the unknowns at the boundaries. Then, inverting equation (22), we easily obtain

$$\mathbf{U}=[H_zH_\theta H_{rk}(\Lambda_{rk}+\Lambda_\theta)^{-1}H_{rk}^{-1}H_\theta^{-1}R^2H_z^{-1}]\mathbf{S}. \tag{23}$$

This method leads to high computing efficiency on vectorial or parallel processors, because they generally incorporate matrix–vector multiplication subroutines.

2.4. *Special treatment for stability improvement*

Let us now consider the implicit part related to the vectorial field $\mathbf{U}(r,\theta,z)$:

$$(\sigma I-\Delta)\mathbf{U}(r,\theta,z)=\mathbf{F}(r,\theta,z),\quad \text{where } (r,\theta,z)\in\,]-1,1]\times[0,2\pi[\,\times[-1,1], \tag{24}$$

with the vectors $\mathbf{U}=(u_r(r,\theta,z),u_\theta(r,\theta,z),u_z(r,\theta,z))$ and $\mathbf{F}=(f_r(r,\theta,z),f_\theta(r,\theta,z),f_z(r,\theta,z))$.

The structure of the vectorial Laplace operator needs to be detailed. Therefore the three Helmholtz problems appear as

$$\sigma u_r-\left[\frac{\partial}{\partial r}\left(\frac{1}{r}\frac{\partial}{\partial r}(ru_r)\right)+\frac{1}{r^2}\frac{\partial^2u_r}{\partial\theta^2}-\frac{2}{r^2}\frac{\partial u_\theta}{\partial\theta}+\left(\frac{\partial^2u_r}{\partial z^2}\right)\right]=f_r, \tag{25}$$

$$\sigma u_\theta-\left[\frac{\partial}{\partial r}\left(\frac{1}{r}\frac{\partial}{\partial r}(ru_\theta)\right)+\frac{1}{r^2}\frac{\partial^2u_\theta}{\partial\theta^2}+\frac{2}{r^2}\frac{\partial u_r}{\partial\theta}+\left(\frac{\partial^2u_\theta}{\partial z^2}\right)\right]=f_\theta, \tag{26}$$

$$\sigma u_z-\left\{\left[\frac{1}{r}\frac{\partial}{\partial r}\left(r\frac{\partial u_z}{\partial r}\right)\right]+\frac{1}{r^2}\frac{\partial^2u_z}{\partial\theta^2}+\left(\frac{\partial^2u_z}{\partial z^2}\right)\right\}=f_z. \tag{27}$$

Obviously, equation (27) has the same structure as the scalar Helmholtz equation (13). However, equations (25) and (26) contain a differential term of first order with respect to θ that couples the two unknowns u_r and u_θ. Neither term can be treated explicitly because of severe stability restrictions. Consequently, the system composed of equations (25) and (26) needs to be manipulated in order to obtain two separate problems. It is then recommended[24] to combine them by setting the new unknowns

$$u_+=u_r+\mathrm{i}u_\theta,\qquad u_-=u_r-\mathrm{i}u_\theta,$$

where u_+ and u_- are two complex functions of the real variables r, θ and z. Thus the knowledge of u_+ is sufficient to furnish the solution $\mathrm{Re}(u_+)=u_r$ and $\mathrm{Im}(u_+)=u_\theta$. Combining (25) + i × (26), we obtain

$$\sigma u_+-\left[\frac{\partial}{\partial r}\left(\frac{1}{r}\frac{\partial}{\partial r}(ru_+)\right)+\frac{1}{r^2}\frac{\partial^2u_+}{\partial\theta^2}+\frac{2i}{r^2}\frac{\partial u_+}{\partial\theta}+\left(\frac{\partial^2u_+}{\partial z^2}\right)\right]=f_r+if_\theta. \tag{28}$$

Let us now consider the procedure of diagonalization as presented in the previous subsection. Although the Laplace operator here appears differently, the first steps of the process are similar. Firstly we diagonalize partially with respect to the direction z. Then the modified version of equation (28) is multiplied by r^2 and the partial diagonalization with respect to the direction r is also of the same type.

Concerning the diagonalization with respect to θ, the differential operator contains an additional first-order term that also has to be diagonalized. The procedure is developed as follows. Set

$$D_\theta=\frac{\partial}{\partial\theta}. \tag{29}$$

The diagonalization is given by

$$D_\theta = C^{-1}\Lambda_\theta C, \tag{30}$$

where Λ_θ is a pure imaginary eigenvalue matrix[16] and the entries of C are

$$c_{kj} = \frac{1}{M}e^{ik\theta_j}, \quad -\frac{M}{2} \leqslant k \leqslant \frac{M}{2} - 1. \tag{31}$$

The differential operator $\partial^2/\partial\theta^2 + 2i\partial/\partial\theta$ present in equation (28) therefore possesses a corresponding discrete matrix that can be represented in the diagonal form

$$C^{-1}(\Lambda_\theta^2 + 2i\Lambda_\theta)C. \tag{32}$$

At this point note that although the entries of C and C^{-1} are complex, the diagonal part of equation (32) is composed of negative real numbers. Finally, equation (28) may be written as

$$[H_z(R^2)^{-1}C^{-1}H_{rz}(\Lambda_{rz} - \Lambda_\theta^2 - 2i\Lambda_\theta)H_{rz}^{-1}CH_z^{-1}]\mathbf{U}_+ = \mathbf{S}_r + i\mathbf{S}_\theta. \tag{33}$$

Inverting equation (33) easily provides the complex unknown vector $\mathbf{U}_+$. The particular form of the eigenvectors in equation (31) allows us to carry out the separation of the real and imaginary parts in equation (33). Consequently, the computation furnishes directly u_r and u_θ using optimal real matrix–vector facilities.

3. SOLVER FOR GENERALIZED STOKES PROBLEM

At this point we are able to solve the scalar and vectorial Helmholtz equations. Now we have to treat their additional coupling with the incompressibility constraint through the pressure field. This leads to the so-called generalized Stokes problem (GSP).

3.1. *The Cahouët and Chabard preconditioning*

Let us study the generalized Stokes problem with Dirichlet-type boundary conditions for velocities. Consider the problem on the velocity field $\mathbf{U}$ and the pressure p that is to be solved in the domain Ω:

$$\begin{aligned} H\mathbf{U} + \nabla p &= \mathbf{F}, \\ \nabla\cdot\mathbf{U} &= 0, \end{aligned} \tag{34}$$

where H is the elliptic Helmholtz operator defined by $H\mathbf{U} = \sigma\mathbf{U} - \Delta\mathbf{U}$, σ is a positive constant related to the time step and $\mathbf{F}$ is a known function obtained by explicit time discretization. Note that H is the Helmholtz operator corresponding to the collocation method described in the previous section, equipped with Dirichlet boundary conditions. Consequently, if p is known, solving equation (34) yields the velocity divergence field

$$\nabla\cdot\mathbf{U} = \nabla\cdot H^{-1}(\mathbf{F} - \nabla p). \tag{35}$$

As a result, the pressure field is the solution of the following problem involving A, the so-called Uzawa operator:

$$Ap = \nabla\cdot H^{-1}(-\nabla p) = s, \tag{36}$$

where s is a source term (known at the time step $n+1$) given by

$$s = \nabla\cdot H^{-1}(-\mathbf{F}). \tag{37}$$

Solving equation (36) is the basic problem of incompressible (or low-Mach-number) flows. In the framework of infinite-order methods (say the general class of spectral methods), numerical experimentation has shown[15,18,20] that the resolution of equation (36) can be reduced to the use of a Poisson solver provided that satisfying boundary conditions on the pressure field can be previously determined. This is the role of the influence matrix technique, which, however, presents severe limitations in the 3D case owing to the huge size of the matrix to be inverted.

Among the remaining rigorous alternatives we have chosen an algorithm, suggested by Cahouët and Chabard,[22] that can be applied to a non-Cartesian geometry. Originally this algorithm was implemented in the framework of finite elements and it can be shown that in a variational formulation the Uzawa operator has a strongly elliptic character.[23] However, this property is not achieved in the present collocation method. Consequently, the conjugate gradient method originally proposed by Cahouët and Chabard[22] cannot be applied and our purpose is to check its global efficiency when minimum residual (MR) or steepest descent (SD) methods are implemented.

Let us now give a description of the algorithm, the aim of which is to carry out a satisfactory preconditioning of system (36). It is a straightforward adaptation of the algorithm in Reference 22.

1. Given p^0, solve $\sigma\mathbf{U}^0 - \Delta\mathbf{U}^0 = f - \nabla p^0$ in Ω and $\mathbf{U}^0 = g_o$) on Γ (Γ is the contour of Ω); compute $r^0 = \nabla\cdot\mathbf{U}^0$.
2. Solve $-\Delta\varphi^0 = r^0$ in Ω and $\partial\varphi^0/\partial n = 0$ on Γ; compute $w^0 = r^0 + \sigma\varphi^0$.
   Then for $m \geq 0$, assuming that p^m, $\mathbf{U}^m$, r^m and w^m are known, compute p^{m+1}, $\mathbf{U}^{m+1}$, r^{m+1} and w^{m+1} as follows.
3. Solve $\sigma\bar{\mathbf{U}}^m - \Delta\bar{\mathbf{U}}^m = -\nabla w^m$ in Ω and $\bar{\mathbf{U}}^m = 0$ on Γ; set $\bar{r}^m = \nabla\cdot\bar{\mathbf{U}}^m$, compute $p^{m+1} = p^m - \rho^m w^m$, $\mathbf{U}^{m+1} = \mathbf{U}^m - \rho^m\bar{\mathbf{U}}^m$ and $r^{m+1} = r^m - \rho^m\bar{r}^m$; solve $-\Delta\bar{\varphi}^m = \bar{r}^m$ in Ω and $\partial\bar{\varphi}^m/\partial n = 0$ on Γ; compute $w^{m+1} = w^m - \rho^m(1 + \sigma\bar{\varphi}^m)$.
4. If r^m is small enough, take $p = p^{m+1}$ and $\mathbf{U} = \mathbf{U}^{m+1}$; do $m = m + 1$ and go back to step 3.

Two relaxation parameters ρ^m have been tested. The steepest descent (SD) method gives

$$\rho^m = \frac{(r^m, w^m)}{(\bar{r}^m, w^m)}, \tag{38a}$$

while the minimum residual (MR) method yields

$$\rho^m = \frac{(r^m, \bar{r}^m)}{(\bar{r}^m, \bar{r}^m)}. \tag{38b}$$

3.2. Convergence properties of the iterative process

As previously mentioned, the quality of the Cahouët and Chabard preconditioning depends on the nature of the discretization. In what follows, we compare our results obtained for different geometries and collocation points with those of Reference 22.

Firstly we study the generalized Stokes problem in the 2D case $[-1, 1] \times [-1, 1]$. We give in Table I the values of the convergence rate for several values of σ in the range 1–1000. This calculation is performed with 45 × 45 Chebyshev collocation nodes for both the SD and MR methods. The rate of convergence, τ, is estimated in the L_∞-norm. More precisely, we compute τ as

$$\tau = \left(\frac{\|\nabla\cdot\mathbf{V}^n\|}{\|\nabla\cdot\mathbf{V}^0\|}\right)^{1/n}, \tag{39}$$

with n fixed at 20 in our study.

A similar study of the convergence rate is performed for the problem in the cube $[-1, 1] \times [-1, 1] \times [-1,1]$. The computation is carried out with 25 × 25 × 25 Chebyshev collocation nodes; σ, the Helmholtz constant, lies in the same range as before.

Table I. Comparison between convergence rates for different geometries versus σ

Method*	$\sigma=1$	$\sigma=10$	$\sigma=100$	$\sigma=1000$
		2D Cartesian case: 45 × 45		
SD	0·61	0·56	0·56	0·52
MR	0·61	0·56	0·56	0·59
		3D Cartesian case: 25 × 25 × 25		
SD	0·68	0·65	0·65	0·62
MR	0·68	0·66	0·66	0·63
		3D cylindrical case: 20 × 16 × 31		
SD(GL)	0·74	0·75	0·75	0·75
SD(GR)	0·69	0·69	0·70	0·71
MR(GL)	0·74	0·74	0·75	0·77
MR(GR)	0·69	0·69	0·70	0·71

* SD, steepest descent; MR, minimum residual; GL, Gauss–Lobatto collocation points; GR, Gauss–Radau collocation points.

Finally, the Stokes problem in the cylindrical domain $]0, 1] \times [0, 2\pi[\times [-1, 1]$ is solved using 20 resp. 31 Chebyshev collocation nodes in the radial resp. vertical direction and 16 Fourier collocation nodes on the azimuth. Let us recall that in the radial direction we have implemented two versions with Gauss–Lobatto and Gauss–Radau points. Both series of results relate to the same numerical conditions as above.

For the sake of comparison, Table I summarizes the convergence rates for all cases. As a general comment, both relaxation methods, SD and MR, yield more or less the same rates and the results are weakly dependent on the value of σ, the Helmholtz constant: the efficiency of the preconditioning increases slightly with σ. However, the dependency of the rate is mainly concerned with the geometry. In the 2D Cartesian geometry we are quite far from the rates of convergence reported in Reference 22. Our calculation involves 2025 pressure nodes, while 1666 are used in the finite element computation of Reference 22. The rates of convergence we have obtained are in the range 0·52–0·61, while the finite element ones are between 0·20 and 0·46.

In the 3D Cartesian geometry the loss of efficiency is also noticeable, although the ranges almost overlap. Our rates of convergence lie within the range 0·62–0·68 and are obtained using 15,625 pressure nodes. In the finite element approach the convergence rate is between 0·30 and 0·58, while the number of pressure nodes remains quite low, 4096.

In the 3D cylindrical geometry the loss of efficiency is even worse. However, the Gauss–Radau chain presents better properties than the Gauss–Lobatto chain as indicated in Tables I and II. For the former set of collocation nodes the convergence rate is close to 0·70 in comparison with 0·75 for the latter, these values being obtained with 9920 pressure nodes.

From the results in Reference 22 it is clear that the proposed preconditioning yields a convergence behaviour independent of the number of pressure nodes. Several tests on coarse and fine grids giving the same rate are reported. This is almost still the case in our study. Sensitivity tests show that the efficiency diminishes very slightly when the discretization increases. For instance, with σ fixed at 1000, we report in Table II a few comparative rates for different discretizations. Because Table II shows a noticeable influence of the number of collocation nodes on the convergence rates, it appears that for a non-equidistant grid the Cahouët and Chabard preconditioning does depend weakly on the discretization. In fact, this is not a surprising result: the Cahouët and Chabard heuristic approach based on Fourier analysis does not apply to non-equidistant grids.

Table II. Effect of degrees of freedom for σ fixed at 1000

Chebyshev collocation			Cahouët and Chabart
2D Cartesian case			
20×20	45×45	65×65	1666 pressure nodes 6502 velocity nodes 3168 elements
$\tau = 0\cdot52$	$\tau = 0\cdot52$	$\tau = 0\cdot57$	$0\cdot20 \leq \tau \leq 0\cdot46$
3D Cartesian case			
$20 \times 20 \times 20$	$35 \times 35 \times 35$		4096 pressure nodes 29791 velocity nodes 20250 elements
$\tau = 0\cdot62$	$\tau = 0\cdot66$		$0\cdot30 \leq \tau \leq 0\cdot57$
Cylindrical case Chebyshev–Fourier collocation			
(GL) $20 \times 16 \times 31$, $\tau = 0\cdot75$ (GR) $20 \times 16 \times 31$, $\tau = 0\cdot71$			(GL) $25 \times 24 \times 31$, $\tau = 0\cdot77$ (GR) $25 \times 24 \times 31$, $\tau = 0\cdot71$

In conclusion, this preconditioning applied to a non-equidistant grid has lost its optimal character. However, even if more work is obviously needed for a cylindrical geometry, our present implementation of this method confirms its practicability.

4. APPLICATION TO DIRECTIONAL SOLIDIFICATION

4.1 Physical considerations

Our purpose is to study in the liquid phase the flow patterns induced by thermosolutal free convection during the directional solidification of a Pb–30%Tl alloy in a cylindrical crucible. The aim is to determine the influence of the convective patterns on the crystal composition at the solid–liquid interface.

For a given pressure the binary alloy phase diagram furnishes solid–liquid equilibria defined by a relationship between temperature and solute composition in both phases. The interfacial ratio of solute concentration in the solid to that in the liquid, the so-called partition coefficient k, appears in the solute conservation condition at the interface and leads to boundary conditions of mixed (Robin) type as generally met in solidification processes. In Table III we give the typical values of the physicochemical properties characterizing the selected alloy, which actually is one of the most experimentally studied.[5,6] Note that Table III does not provide four important parameters that control the liquid phase flow. These quantities depend directly on V_0, the drawing velocity (or growth velocity), which is an external parameter imposed on the crucible. This allows us to define the solutal length (i.e. the typical length of scale of the concentration gradient)

$$l_S = \frac{D}{V_0}, \tag{40}$$

the reduced radius of the crucible,

$$\beta = \frac{R}{l_S}, \tag{41}$$

Table III. Physicochemical parameters for Pb–30% Tl alloy

Parameter	Value
D	2×10^{-5} cm^2 s^{-1}
D_{th}	$0{\cdot}108$ cm^2 s^{-1}
α_C	$-5{\cdot}4 \times 10^{-4}$ wt.%$^{-1}$
α_T	$1{\cdot}15 \times 10^{-4}$ K^{-1}
ν	$2{\cdot}43 \times 10^{-3}$ cm^2 s^{-1}
K_L	$0{\cdot}155$ J cm^{-1} K^{-1} s^{-1}
K_S	$0{\cdot}314$ J cm^{-1} K^{-1} s^{-1}
k	1·1
Sc	121·5
Pr	0·0225
Le	5400

the solutal Rayleigh number

$$R_S = \frac{\alpha_C g C_\infty (1-k)}{k\eta D} l_S^3, \tag{42}$$

the thermal Rayleigh number

$$R_T = \frac{\alpha_T g \Delta T}{\eta D} l_S^3, \tag{43}$$

the Schmidt number

$$Sc = \frac{\eta}{D} \tag{44}$$

and the Lewis number

$$Le = \frac{D_{th}}{D}, \tag{45}$$

where α_C and α_T are the solutal and thermal expansion coefficients respectively, η is the kinematic viscosity, D_{th} is the coefficient of thermal diffusivity, R is the radius of the cylinder and g is the gravitational acceleration. At this point let us recall our choice for getting the non-dimensional set of equations given by (1)–(4) of Section 2. The velocity, length and temperature are reduced with V_0, l_S and ΔT respectively, where ΔT is the temperature drop imposed on the liquid cylinder. The concentration is expressed in terms of the drop in thallium mass fraction reduced with $\Delta C = C_\infty (k-1)/k$, where ΔC is the drop in thallium mass fraction given by the diffusive solution,[26] C_∞ being the thallium mass fraction in the liquid phase far from the interface (i.e. $C_\infty = 30\%$). We now specify the boundary conditions added to equations (1)–(4) of Section 2.

1. For the velocity field we impose no-slip boundary conditions on the whole contour for u_r resp. u_θ, the radial resp. azimuthal component. The axial component u_z is set on the whole contour to $-V_0$, the opposite of the growth velocity.
2. For the concentration field we impose a Dirichlet condition at the top of the cylindrical domain, a homogeneous Neumann condition on the lateral wall and the following solute conservation condition at the bottom of the cylinder:

$$D\frac{\partial C}{\partial z} + (1-k)V_0 C = 0. \tag{46}$$

3. For the temperature field we impose Dirichlet conditions T_m at the bottom of the cylinder (T_m corresponds to the fusion temperature) and $T_m + \Delta T$ at the top. For the lateral wall we choose a homogeneous Neumann condition (hypothesis of adiabatic crucible).

We start the time integration with different types of initial condition. We study the flow patterns obtained either by destabilization of the diffusive solution or by modification of a solution previously computed with a less stiff set of parameters.

4.2 Results and discussion

In order to illustrate the applicability of the method, we present for an intermediate value of the aspect ratio ($\beta = 5$) the hydrodynamic analysis of two different configurations of 3D flows and their influence on the composition in the solid phase. The selected illustrations are concerned with two important regimes of flow: the axisymmetric and non-axisymmetric patterns. The former is obtained for low solutal Rayleigh number: the presented example corresponds to $R_S = 40$. For the non-axisymmetric flow the illustration is for $R_S = 60$.

The simplicity of the pattern for the first example leads to a rather easy flow analysis. Figure 1(a) presents the level contours of the axial component of the velocity drawn in the horizontal plane $z = 6{\cdot}6$ and shows that the flow is axisymmetric. Figure 1(b) shows a similar plot of the same field drawn in the vertical plane $\theta = 0$. This indicates that the flow penetrates the liquid to a typical height of about 20 times the solutal length. For the reduced composition field, Figure 2(a) shows the iso-concentration lines drawn in the vertical plane $\theta = 0$. In this plot it is noticeable that most of the lines are confined close to the crystal in a domain of thickness unity, confirming that l_S, the solutal length, is the basic length scale of the problem. A blow-up of this domain is shown in Figure 2(b), where it can be

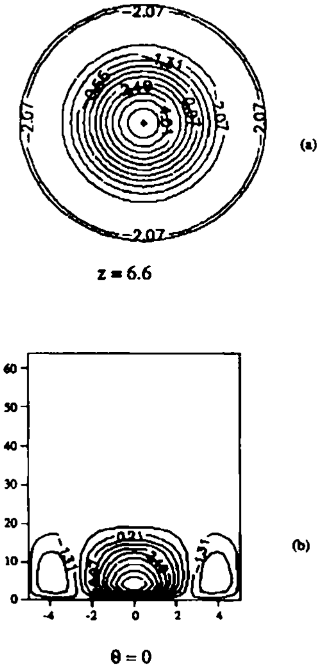

Figure 1. Level contours of axial component of velocity in (a) horizontal plane $z = 6{\cdot}6$ and (b) vertical plane $\theta = 0$ for $\beta = 5$, $R_S = 40$

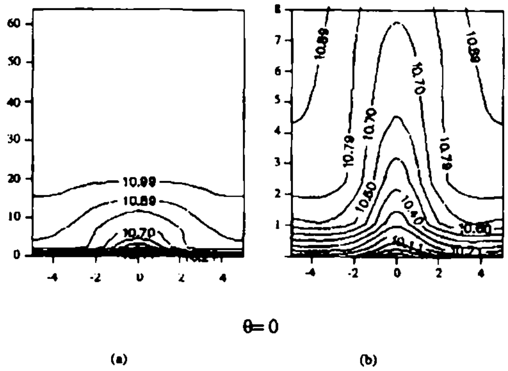

Figure 2. (a) Iso-concentration lines in vertical plane $\theta = 0$ for $\beta = 5$, $R_S = 40$. (b) Blow-up of (a) above solid–liquid interface

observed that the composition of the liquid phase is impoverished in thallium along the cylinder axis. According to Figure 1(b), the flow is ascending along the axis.

This set of observations is consistent with the fact that the solid phase contains more thallium than the liquid, leading to a lighter fluid close to the interface. The analysis shows that the role of the convective flow is to feed with thallium the liquid composition at the interface (or, in an equivalent way, to carry far from the interface the excess of lead rejected from the solid phase). Consequently, the crystal does not grow in a uniform fluid composition: where the flow descends the crystal has to be in phase equilibrium with a liquid richer in thallium. Therefore its composition presents a radial dependence as illustrated in Figure 3, which shows the level contours of the crystal composition deduced from the liquid composition at the interface. We can see that at the centre the magnitude of the thallium drop is about 3·3%. This result is in agreement with experiments showing a radial dependence of the same amplitude.[6]

To illustrate the non-axisymmetric flow, we set $R_S = 60$. The flow pattern we have obtained for this parameter presents a unique convective roll (leading to an azimuthal dependence corresponding to the first Fourier mode). This flow has a plane of symmetry near $\theta = \pi/2$. Figure 4(a) presents the level contours of the axial component of this convective roll, drawn in the horizontal plane $z = 6{\cdot}6$. It illustrates that in this horizontal plane the flow possesses the already mentioned symmetry. Figure 4(b) shows the same field plotted in the vertical plane $\theta = \pi/2$, which contains the locus of the maximum of the vertical velocity. In this case the flow penetration involves the whole computational domain. This addresses the following issue: is the cylinder sufficiently high in our simulation? As a result, the height

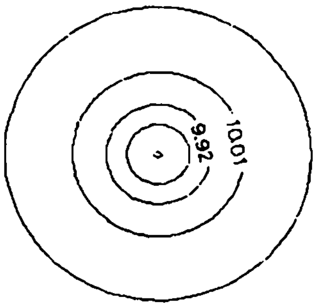

Figure 3. Level contours of reduced solute composition in horizontal plane $z = 0$ (interface) for $\beta = 5$, $R_S = 40$

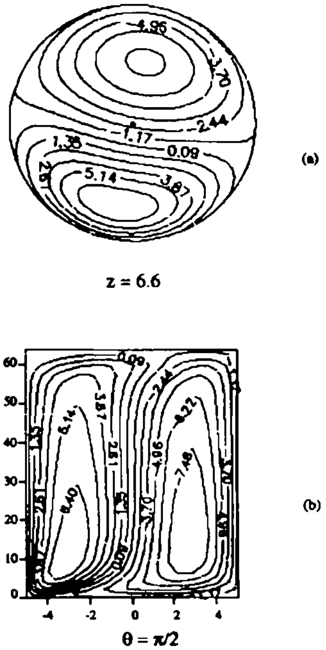

Figure 4. Level contours of axial component of velocity in (a) horizontal planes $z = 6{\cdot}6$ and (b) vertical plane $\theta = \pi/2$ for $\beta = 5, R_S = 60$

of the cylinder has a weak influence on the crystal composition as long as no boundary layer of solute concentration appears at the top of the cylinder. In Figure 5(a) we verify that this is the case. This figure presents the iso-concentration lines drawn in the vertical plane $\theta = \pi/2$. This plot is, however, of weak physical significance because all lines are confined in a layer of thickness unity. A blow-up of this layer is shown in Figure 5(b), where it can be observed that as in the previous case the composition of the liquid phase is modified by the ascending or descending column.

To study the crystal composition, we analyse the reduced thallium mass fraction at the interface. Figure 6 shows the level contours of the latter quantity drawn in the plane of the interface ($z = 0$). The plots are in agreement with the observation of ascending and descending columns in Figures 4(a) and 4(b). As a matter of fact, the maximum of the thallium species is located close to the centre, while its minimum appears in a specific zone situated on the crystal boundary. This minimum is actually the

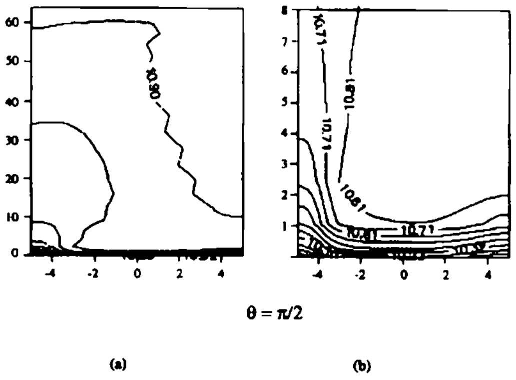

Figure 5. (a) Iso-concentration lines in vertical plane $\theta = \pi/2$ for $\beta = 5$, $R_S = 60$. (b) Blow-up of (a) above solid–liquid interface

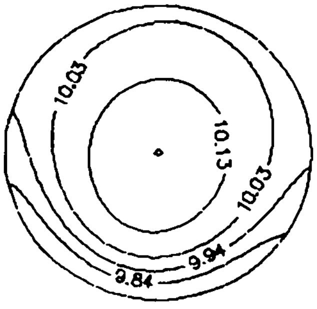

Figure 6. Level contours reduced solute composition in horizontal plane $z = 0$ (interface) for $\beta = 5$, $R_S = 60$

result of two co-operative effects. On the one hand this zone is affected by the proximity of the ascending column. On the other hand the points close to the crystal sides grow from a liquid phase weakly renewed because of the viscous boundary layers.

The latter effect was already present in the previous axisymmetric case. A more precise plot of the thallium mass fraction along a diameter in the crystal is shown in Figure 7(a) for $R_S = 40$. Note that here the thallium mass fraction of the crystal is the non-reduced quantity. One observes that the renewal effect of the descending fountain is also damped in the vicinity of the cylinder wall. We additionally notice that the amplitude of the thallium fluctuation in the crystal is about 0·96%. The same plot for the non-axisymmetric case is presented in Figure 7(b). The crystal composition seems to

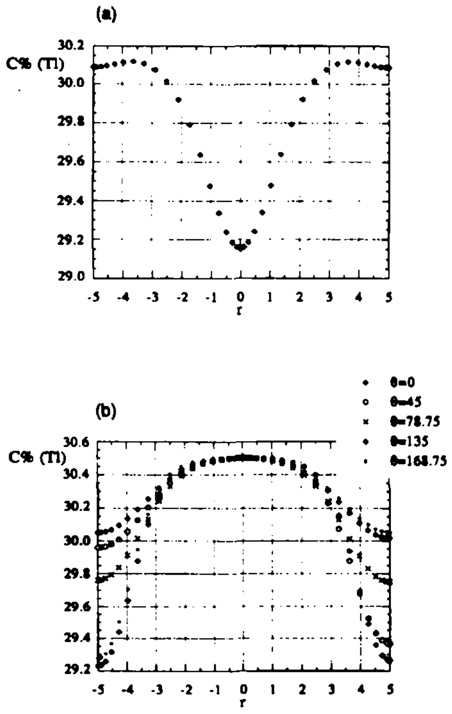

Figure 7. Variation in non-reduced thallium composition in solid at interface versus radius of cylinder for (a) $\beta = 5$, $R_S = 40$ and (b) $\beta = 5$, $R_S = 60$

be more uniform, especially around the centre, although the amplitude of the fluctuation is larger. We measure a 1·27% variation in the thallium composition in the crystal.

5. CONCLUSIONS

We have presented a high-accuracy numerical method to solve the thermosolutal convective flow induced by vertical Bridgman directional solidification. The space discretization is based on a Chebyshev–Fourier collocation method applied on the primitive variables. The incompressibility constraint has been enforced using an iterative resolution of the Uzawa operator giving the related pressure field. This iterative technique uses the preconditioning recommended by Cahouët and Chabard.[22] We have established that the efficiency of this technique applied to our high-order method becomes lower than for the results obtained with finite elements. Two reasons have been put forward. On the one hand, collocation methods do not provide a symmetric Uzawa operator. Consequently, the procedure cannot take advantage of the conjugate gradient method. On the other hand the Fourier analysis had provided a fairly good heuristic guide to the previous preconditioning.[22] It seems clear that in a cylindrical geometry such an analysis could not retain its efficiency. Note that in the radial direction the Gauss–Radau collocation points provides slightly better results than the Gauss–Lobatto ones. Nevertheless, for the time being, this preconditioning allowed us to rigorously enforce the incompressibility condition. Although the convergence rate is quite feeble, we have found this method practicable. Concerning both illustrations presented above, the maximum of the divergence field when the steady solutions are reached is about 10^{-5}, the number of iterations on the Uzawa operator being limited to six at each time step.

In the application to directional solidification we have shown that the considerable expanded effort in computing the flows is not wasted, because we have numerically predicted relatively large fluctuations in the crystal composition. In both illustrations at moderate Rayleigh numbers that we have presented, a binary alloy grows from a Pb–30% Tl liquid phase. The resulting crystal is in fact a non-homogeneous alloy with 29·2%–30·1% mass fraction of thallium for axisymmetric flow and 29·2%–30·5% for non-axisymmetric flow.

ACKNOWLEDGEMENT

This work has been supported by a grant from the Scientific Council of the CNIMAT (Project 014A94a), Nancy, France.

REFERENCES

1. D. T. J Hurle, in E. Kaldis and J. H. Scheel (eds), *Crystal Growth and Materials*, North-Holland, Amsterdam 1977, p. 550.
2. M. A. Azouni, *PhysicoChem. Hydrodyn.*, **2**, 295 (1981).
3. S. M. Pimputkar and S. Ostrach, *J. Crystal Growth*, **55**, 614 (1981).
4. M. E. Glicksman, S. R. Coriell and G. B. McFadden, *Ann. Rev. Fluid Mech.*, **18**, 307 (1986).
5. H. Nguyen Thi, B. Billia and H. Jamgotchian, *J. Fluid Mech.*, **204**, 581–597 (1989).
6. H. Jamgotchian, B. Billia and L. Capella, *J. Cryst. Growth*, **82**, 342–350 (1987).
7. S. R. Coriell, G. B. McFadden and R. F. Sekerka, *Ann. Rev. Mater. Sci.*, **15**, 119 (1985).
8. R. J. Schaefer and S. R. Coriell, *Metall. Trans. A*, **15**, 2109 (1984).
9. M. Hicham Ettouney and R. Brown, *J. Comput. Phys.*, **49**, 118–150 (1983).
10. J. Chiechun Chang and R. Brown, *J. Comput. Phys.*, **53**, 1–27 (1984).
11. E. Crespo Del Arco and P. Bontoux, *Phys. Fluids A*, **1**, 1348–1359 (1989).
12. D. Gottlieb and S. A. Orszag, *Numerical Analysis of Spectral Methods: Theory and Applications*, SIAM–CBMS, Philadelphia, PA, 1977.
13. J. P. Pulicani and J. Ouzzani, *Comput. Fluids*, **20**, 93–109 (1991).
14. J. P. Pulicani, E, Crespo Del Arco, A. Randriamanpianina, P. Bontoux and R. Peyret, *Int. j. numer. methods fluids*, **10**, 481–517 (1990).

15. U. Ehrenstein and R. Peyret, *Int. j. numer. methods fluids*, **9**, 427–452 (1989).
16. C. Canuto, M. Y. Hussaini, A. Quarteroni and T. A. Zang, *Spectral Methods in Fluid Dynamics*, Springer, Berlin, 1987.
17. D. Gottlieb, M. Y. Hussaini and S. A. Orszag. 'Theory and application of spectral methods', in R. G. Voigt, D. Gottlieb and M. Y. Hussaini (eds), *Spectral Methods for Partial Differential Equations*, SIAM–CBMS, Philadelphia, PA, 1984, pp. 1–54.
18. L. Kleiser and U. Schumann, in E. H. Hirschel (ed.), *Proc. Third GAMM Conf. on Numerical Methods in Fluid Mechanics*, Vieweg, Braunschweig, p. 165, 1980.
19. L. Tuckerman, *J. Comput. Phys.*, **80**, 403–441 (1989).
20. P. Le Quéré and J. Pécheux, *Comput. Methods Appl. Mech. Eng.*, **80**, 261–271 (1990).
21. P. Haldenwang, Thèse d'Etat, Université de Provence, 1984, unpublished; *ASME/HTD*, **60**, 45–51 (1986).
22. J. Cahouët and J. P. Chabard, *Int. j. numer. methods fluids*, **8**, 869–895 (1988).
23. R. Glowinski, *J. Comput. Phys.*, **103**, 189–221 (1992).
24. A. T. Patera and S. A. Orszag, in A. R. Bishop, D. K. Campbell and B. Nicolaenko (eds), *Non linear Problems: Present and Future*, North-Holland, Amsterdam, 1982, p. 367.
25. P. Haldenwang, G. Labrosse, S. Abboudi and M. Deville, *J. Comput. Phys.*, **55**, 115–128 (1984).
26. R. Z. Guérin, B. Billia and P. Haldenwang, *Phys. Fluids A*, 3, 1873–1879 (1991).